nature nanotechnology

LETTERS

https://doi.org/10.1038/s41565-021-01004-0

Dual-coupling-guided epitaxial growth of wafer-scale single-crystal WS_2 monolayer on vicinal *a*-plane sapphire

Jinhuan Wang[1,2,16], Xiaozhi Xu[3,16], Ting Cheng[4,5,16], Lehua Gu[6,16], Ruixi Qiao[1,7], Zhihua Liang[3], Dongdong Ding[1], Hao Hong[1,8], Peiming Zheng[3], Zhibin Zhang[1], Zhihong Zhang[1], Shuai Zhang[9], Guoliang Cui[3], Chao Chang[3], Chen Huang[1], Jiajie Qi[1], Jing Liang[1], Can Liu[1], Yonggang Zuo[1], Guodong Xue[1], Xinjie Fang[1], Jinpeng Tian[10], Muhong Wu[7], Yi Guo[1], Zhixin Yao[11], Qingze Jiao[2], Lei Liu[11], Peng Gao[7], Qunyang Li[9], Rong Yang[10], Guangyu Zhang[10,12], Zhilie Tang[3], Dapeng Yu[13], Enge Wang[7,12,14], Jianming Lu[1], Yun Zhao[2] ✉, Shiwei Wu[6] ✉, Feng Ding[4,15] ✉ and Kaihui Liu[1,7,12] ✉

The growth of wafer-scale single-crystal two-dimensional transition metal dichalcogenides (TMDs) on insulating substrates is critically important for a variety of high-end applications[1-4]. Although the epitaxial growth of wafer-scale graphene and hexagonal boron nitride on metal surfaces has been reported[5-8], these techniques are not applicable for growing TMDs on insulating substrates because of substantial differences in growth kinetics. Thus, despite great efforts[9-20], the direct growth of wafer-scale single-crystal TMDs on insulating substrates is yet to be realized. Here we report the successful epitaxial growth of two-inch single-crystal WS_2 monolayer films on vicinal *a*-plane sapphire surfaces. In-depth characterizations and theoretical calculations reveal that the epitaxy is driven by a dual-coupling-guided mechanism, where the sapphire plane–WS_2 interaction leads to two preferred antiparallel orientations of the WS_2 crystal, and sapphire step edge–WS_2 interaction breaks the symmetry of the antiparallel orientations. These two interactions result in the unidirectional alignment of nearly all the WS_2 islands. The unidirectional alignment and seamless stitching of WS_2 islands are illustrated via multiscale characterization techniques; the high quality of WS_2 monolayers is further evidenced by a photoluminescent circular helicity of ~55%, comparable to that of exfoliated WS_2 flakes. Our findings offer the opportunity to boost the production of wafer-scale single crystals of a broad range of two-dimensional materials on insulators, paving the way to applications in integrated devices.

Wafer-scale single-crystal films of two-dimensional (2D) transition metal dichalcogenides (TMDs) are essential for high-end device applications. The seamless coalescence of millions of unidirectionally aligned 2D islands on a single-crystal substrate has been proven to be a suitable method for the growth of wafer-scale 2D single crystals[5–8]. However, in the case of TMDs, the direct growth of monolayer single-crystal films on a wafer-scale insulating substrate has not been achieved in spite of some progress in orientation control in the past decade[9,10]. The challenge is mainly because of the non-centrosymmetric C_{3v} lattice of TMDs, which generally leads to the equivalency of antiparallel islands on most high-symmetry surfaces[15]. Hence, new methods need to be developed for the unidirectional alignment of TMD islands on insulators.

In principle, as TMDs and hexagonal boron nitride (hBN) lattices have the same in-plane symmetry, the successful epitaxy of 2D hBN can offer important clues to obtain large-area epitaxial TMD single crystals[6–8]. However, the unidirectional alignment of hBN islands was achieved on metallic substrates by taking advantage of the strong coupling between the hBN edge and step edge on the transition metal surface. Such a strong edge–step edge coupling may not be feasible when growing TMDs on an insulating surface because of the self-passivation of the TMD edge and the inert surface of the insulator[21,22]. Therefore, the mechanism of the epitaxy of

[1]State Key Laboratory for Mesoscopic Physics, Frontiers Science Center for Nano-optoelectronics, School of Physics, Peking University, Beijing, China. [2]School of Chemistry and Chemical Engineering, Beijing Institute of Technology, Beijing, China. [3]Guangdong Provincial Key Laboratory of Quantum Engineering and Quantum Materials, Guangdong-Hong Kong Joint Laboratory of Quantum Matter, School of Physics and Telecommunication Engineering, South China Normal University, Guangzhou, China. [4]Center for Multidimensional Carbon Materials, Institute for Basic Science, Ulsan, Korea. [5]College of Chemistry and Molecular Engineering, Academy for Advanced Interdisciplinary Studies, Peking University, Beijing, China. [6]State Key Laboratory of Surface Physics and Department of Physics, Fudan University, Shanghai, China. [7]International Center for Quantum Materials, Collaborative Innovation Center of Quantum Matter, Peking University, Beijing, China. [8]Interdisciplinary Institute of Light-Element Quantum Materials and Research Center for Light-Element Advanced Materials, Peking University, Beijing, China. [9]Department of Engineering Mechanics, State Key Laboratory of Tribology, Tsinghua University, Beijing, China. [10]Nanoscale Physics and Devices Laboratory, Institute of Physics, Chinese Academy of Sciences, Beijing, China. [11]School of Materials Science and Engineering, Peking University, Beijing, China. [12]Songshan Lake Materials Laboratory, Institute of Physics, Chinese Academy of Sciences, Guangdong, China. [13]Shenzhen Institute for Quantum Science and Engineering, and Department of Physics, Southern University of Science and Technology, Shenzhen, China. [14]School of Physics, Liaoning University, Shenyang, China. [15]School of Materials Science and Engineering, Ulsan National Institute of Science and Technology, Ulsan, Korea. [16]These authors contributed equally: Jinhuan Wang, Xiaozhi Xu, Ting Cheng, Lehua Gu. ✉e-mail: zhaoyun@bit.edu.cn; swwu@fudan.edu.cn; f.ding@unist.ac.kr; khliu@pku.edu.cn

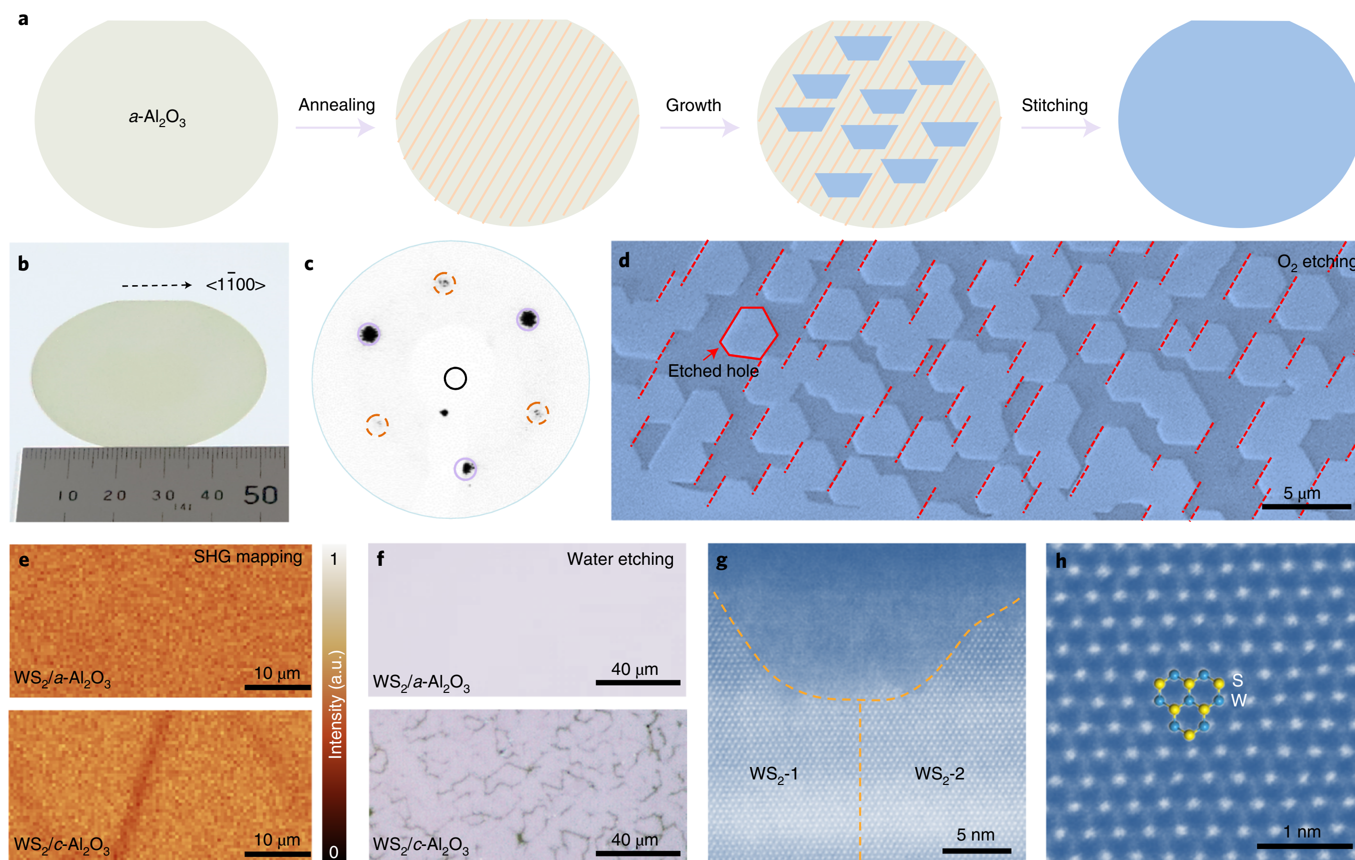

Fig. 1 | Growth and characterization of single-crystal WS_2 monolayer on vicinal *a*-plane sapphire. **a**, Schematic of the growth process of a WS_2 monolayer on vicinal *a*-plane sapphire (abbreviated as *a*-Al_2O_3). **b**, Photograph of the as-grown full-coverage WS_2 monolayer on a two-inch sapphire wafer. The direction of the straight edge is $<1\bar{1}00>$. **c**, Representative LEED pattern of the WS_2 film (as measured at position 1 shown in Supplementary Fig. 6a). Due to the three-fold rotational symmetry, three diffraction spots have a higher intensity (solid violet circles) than three other spots (dashed orange circles). **d**, False-colour SEM image of WS_2 films after O_2 etching. The etched holes have similar shapes and the same orientation. **e**, SHG mapping of WS_2 grown on *a*-Al_2O_3 (top) and *c*-Al_2O_3 (bottom). **f**, Optical images of WS_2 film grown on *a*-Al_2O_3 (top) and *c*-Al_2O_3 (bottom) after hot water vapour etching. No boundaries are observed for WS_2/*a*-Al_2O_3, but boundaries can be clearly seen in WS_2/*c*-Al_2O_3. **g**, Atomically resolved STEM image from the merged area of the two aligned WS_2 islands (namely, WS_2-1 and WS_2-2), showing that no boundary was formed. **h**, Atomically resolved STEM image of the high-quality WS_2 lattice.

2D TMDs on an insulating surface might be substantially different from that on a metal surface.

Here we demonstrate a few rules as guidelines to choose a proper insulating substrate. First, the insulating surface should have low symmetry to break the energy degeneracy of two antiparallel TMD islands[23]. Second, it should be possible to obtain an atomically flat surface with uniformity on the wafer scale and thereby ensure a uniform, intimate contact between the 2D materials and the substrate. Referring to the established growth philosophy of aligned carbon nanotubes on sapphire[24], we decided to employ a single-crystal sapphire substrate cut along a plane that has a very small angle from the $(11\bar{2}0)$ surface, or vicinal *a*-plane sapphire (referred to as *a*-Al_2O_3, if not specified otherwise). This kind of sapphire substrate was custom-designed and fabricated by a local supplier, which allowed us to obtain *a*-Al_2O_3 with a cutting angle as small as 0.1° along a certain direction (Methods and Supplementary Figs. 1 and 2 provide details).

The sapphire substrates were first annealed in an oxygen (O_2) atmosphere at a high temperature to stabilize the parallel atomic steps, which typically have a width of 350 nm and height of 2 Å on the surface (Supplementary Fig. 3). These atomic step edges are designed to break the C_2 symmetry of *a*-plane sapphire and guide the unidirectional alignment of WS_2 islands for the epitaxial growth of the single-crystal monolayer film (Fig. 1a). The prevailing recipe for WS_2 monolayer growth was adopted (Methods), and a complete WS_2 monolayer film on a two-inch sapphire wafer was successfully synthesized (Fig. 1b and Supplementary Figs. 4 and 5).

To evaluate whether the film is formed by unidirectionally aligned WS_2 domains, characterizations including low-energy electron diffraction (LEED), second-harmonic generation (SHG) and O_2 etching were performed. Three diffraction spots have a higher intensity (indicated by solid violet circles in Fig. 1c) than three other spots (indicated by dashed orange circles in Fig. 1c) due to the three-fold rotational symmetry of WS_2, which is strong proof of the unidirectional alignment of different domains in the film (Fig. 1c and Supplementary Fig. 6). The parallelly aligned holes in the WS_2 film after O_2 etching (Fig. 1d, Supplementary Fig. 7a–d for single-crystal WS_2, and Supplementary Fig. 8 for polycrystalline WS_2), as well as the nearly identical polarization-dependent SHG patterns (Supplementary Fig. 7e–h), further confirmed that the film has no misaligned domains.

Several characterization techniques ranging from the macroscopic scale to the atomic scale have been used to confirm that parallel WS_2 islands were seamlessly stitched together without forming grain boundaries. In the large scale, the grain boundaries could be visualized by SHG mapping[25] (destructive interference at the

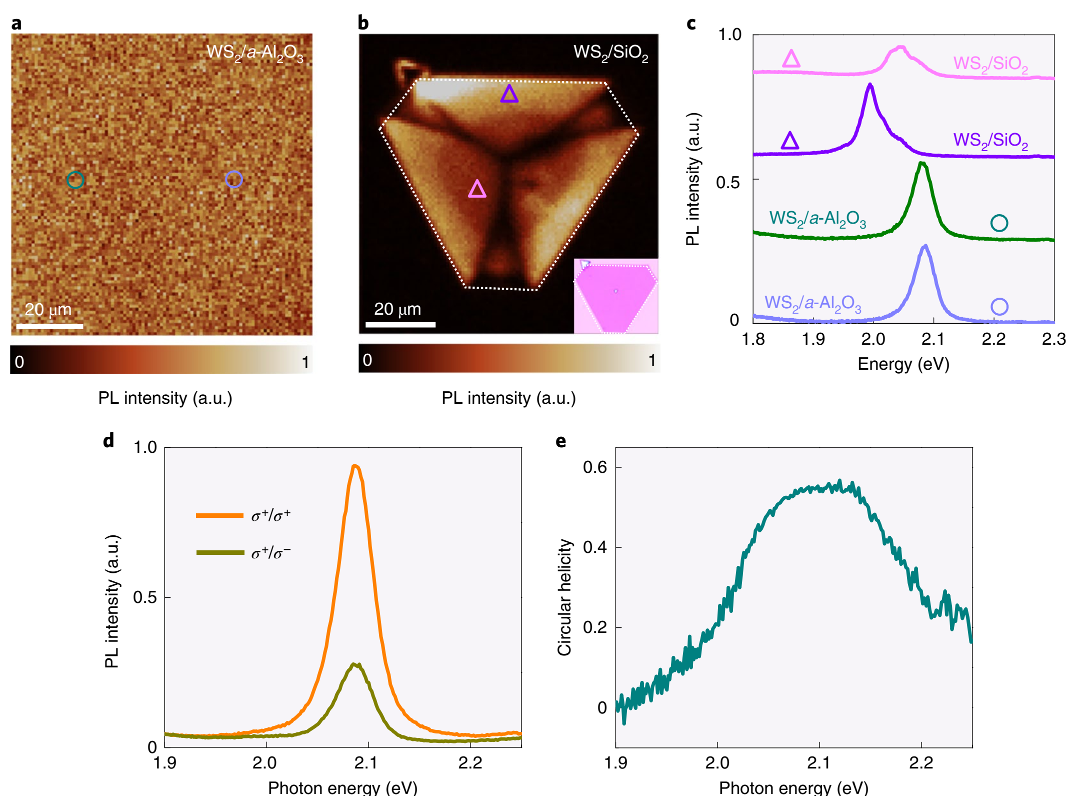

Fig. 2 | High-quality WS_2 monolayer grown on vicinal *a*-plane sapphire. a, Typical PL mapping of a WS_2 film grown on *a*-Al_2O_3. The PL intensity is uniform in the whole area. **b**, Typical PL mapping of a single-crystal WS_2 island grown on SiO_2/Si substrate. Inset: optical image of the WS_2 domain in **b**. **c**, PL spectra of WS_2 at the positions marked by circles and triangles in **a** and **b**. Many side peaks that can be assigned to trion and defect states are observed for WS_2/SiO_2. Further, the PL spectra of WS_2/*a*-Al_2O_3 show a single narrow peak corresponding to the exciton state in high-quality materials. **d**, Circularly polarized PL spectra of WS_2 grown on *a*-plane sapphire. The excitation light is right-handed (σ^+) circularly polarized at 2.34 eV. Left-handed (σ^-) and right-handed (σ^+) circularly polarized PL spectra are shown in dark yellow and orange, respectively. **e**, Circular helicity calculated from the PL spectra in **d**. The high value over 55% indicates the high quality of our WS_2 monolayer. All the PL spectra and mappings were measured at 7.5 K.

boundary shows dark lines) or hot water vapour etching (the defective boundaries are etched to show dark lines). For the WS_2 film grown on *a*-Al_2O_3, no boundaries were observed in either SHG mapping (Fig. 1e, top, and Supplementary Fig. 9a,b) or water etching mapping (Fig. 1f, top). In contrast, obvious boundaries appeared for the film grown on the *c*-Al_2O_3 surface[15] (Fig. 1e, bottom; Supplementary Fig. 9c,d for SHG mapping; and Fig. 1f, bottom, for water etching). In Fig. 1g,h, the aberration-corrected transmission electron microscopy (TEM) image and dark-field TEM image clearly showed atomic evidence of the seamless stitching between adjacent WS_2 islands (Supplementary Figs. 10 and 11 provide further details). Theoretically, our calculations demonstrated that forming a perfect WS_2 crystal lattice between two parallelly aligned WS_2 islands is much more energetically preferred than forming grain boundaries (Supplementary Figs. 12 and 13); this perfect grain stitching has also been experimentally demonstrated during the coalescence of other 2D materials of graphene and hBN (refs. [5,6]). However, it is actually very difficult to identify all the defects through two-inch films, as existing characterization techniques are limited to a very small area. Therefore, WS_2 films may contain line defects in the coalescence of millions of islands.

The exceptionally high quality of the obtained large-area single-crystal WS_2 monolayer was demonstrated using several different characterization techniques. First, a statistical analysis of the atomic aberration-corrected TEM images showed that the grown WS_2 is of high quality with a sulfur (S) vacancy concentration of ~0.05 per square nanometre, which is about half of the reported values[26,27] (Supplementary Fig. 14). Second, the low-temperature photoluminescence (PL) map of the WS_2 film grown on *a*-Al_2O_3 shows extremely uniform intensity (Fig. 2a), with a narrow distribution of peak widths and identical peak energy at different positions on the sample (Fig. 2c). In comparison, the PL map of a WS_2 island grown on SiO_2/Si substrates has a non-uniform intensity distribution and both peak widths and energies of the PL spectra depend on the location (Fig. 2b,c). The identical PL peak in our WS_2/*a*-Al_2O_3 is assigned to the pure exciton state in a high-quality material, whereas the side peaks in WS_2/SiO_2 are assigned to trion and defect states in a relatively lower-quality material[28].

Third, our WS_2/*a*-Al_2O_3 had a very high circular helicity in the circularly polarized PL spectrum, another strong proof of its high quality, since the circular helicity arises from the valley freedom at the K and K' points of the Brillouin zone and is very sensitive to any defect that will introduce intervalley scattering to degrade the circular helicity[29]. For high-quality WS_2 monolayer flakes exfoliated from high-quality bulk single crystals, the measured circular helicity ($\rho = \frac{I_+ - I_-}{I_+ + I_-}$, where $I_\pm$ is the intensity of the $\sigma^\pm$ PL components) was generally lower than 40% (refs. [30–32]), and the as-grown WS_2 monolayer on SiO_2/Si had typical circular helicity lower than 20% (Supplementary Fig. 15a,b). Strikingly, our WS_2/*a*-Al_2O_3 had circular helicity up to 55% (Fig. 2d,e), competitive to those of the best exfoliated flakes.

Last, we checked the quality by electrical measurements. We first fabricated field-effect transistor (FET) devices following standard procedures with back-gate geometry. The results showed that

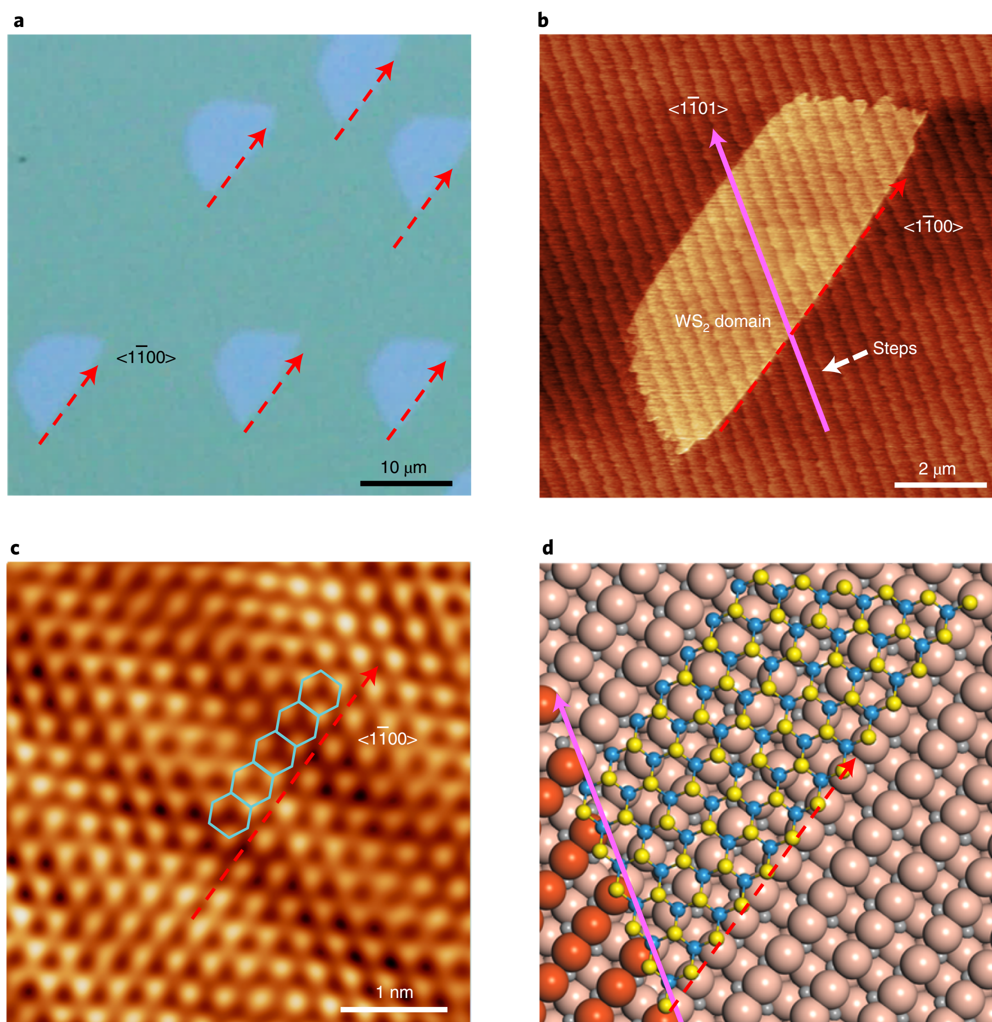

Fig. 3 | Characterization of WS_2 islands on vicinal *a*-plane sapphire. **a**, Optical image of individual WS_2 islands on *a*-Al_2O_3. All the islands are trapezoidal in shape with long edges along the <1$\bar{1}$00> direction of sapphire. **b**, AFM image of a WS_2 island. The direction of the Al_2O_3 steps is <1$\bar{1}$01>. **c**, Zoomed-in atomically resolved AFM image of the WS_2 sample shown in **b**. The long zigzag edge of the hexagonal lattice of WS_2 is along the <1$\bar{1}$00> direction. **d**, Schematic of the atomic geometry of WS_2/*a*-Al_2O_3. The red and brown balls correspond to the first and second layer of O atoms from the surface, respectively. The grey balls correspond to Al atoms.

mobility of the WS_2 sample was about 0.8–1.6 $cm^2 (V s)^{-1}$ at room temperature (Supplementary Fig. 16a). This value is not very high as the quality of electrode contact of WS_2 is usually very poor, which greatly affects the measured mobility value. To check this assumption, we also fabricated FET devices with exfoliated WS_2 monolayers using the same procedures, and the results showed that the measured mobility of exfoliated WS_2 was not high as ~1.0–1.9 $cm^2 (V s)^{-1}$ (Supplementary Fig. 16b). To reduce the influence of electrode contact, we further fabricated ionic-liquid-gate FET and measured its electrical transport properties[33]. The result showed that our WS_2 samples have a relatively large carrier mobility of ~50 $cm^2 (V s)^{-1}$ at 150 K (Supplementary Fig. 16c,d).

To deeply understand the mechanism of single-crystal WS_2 growth on the vicinal *a*-plane sapphire, we showed that the WS_2 islands formed in the initial stages of growth, as shown in Fig. 3a, where unidirectionally aligned islands—all of them having the same trapezoidal shape—are clearly seen. High-resolution atomic force microscopy (AFM) images of a typical WS_2 island further confirm the presence of parallel step edges as well as crystallinity (Fig. 3b,c). The longest edge of the trapezoidal WS_2 island is a zigzag edge along the <1$\bar{1}$00> direction of sapphire (Supplementary Figs. 17 and 18 provide details of the formation mechanism), rather than along the step-edge direction of <1$\bar{1}$01> of the sapphire surface. To confirm the epitaxial relationship of WS_2/*a*-Al_2O_3, glancing-angle X-ray diffraction was conducted and the result shows that the zigzag edge of WS_2 is parallel to the <1$\bar{1}$00> direction of *a*-Al_2O_3, which is consistent with our optical and AFM characterizations (Supplementary Fig. 19). This scenario is totally different from the step-edge-guided growth of hBN on vicinal Cu(110) surfaces, where the longest edge of a trapezoidal hBN island is tightly bound to the <211> step edge of the Cu surface[6]. Thus, we believe that the mechanism of the unidirectional alignment of WS_2 islands on the *a*-Al_2O_3 surface must be different from that of the alignment of graphene and hBN on metal surfaces.

Based on our theoretical analysis and density functional theory (DFT) calculations, we discover that the epitaxial alignment of WS_2 islands on the *a*-Al_2O_3 surface is governed by a dual-coupling-guided mechanism. The first driving force is the coupling between WS_2 and *a*-plane sapphire, which leads to two energetically degenerated antiparallel alignments of WS_2 islands (Fig. 4a,b and Fig. 4c, top). The second driving force is the coupling between WS_2 and the step edges of sapphire, where the step edges serve as active lines of the

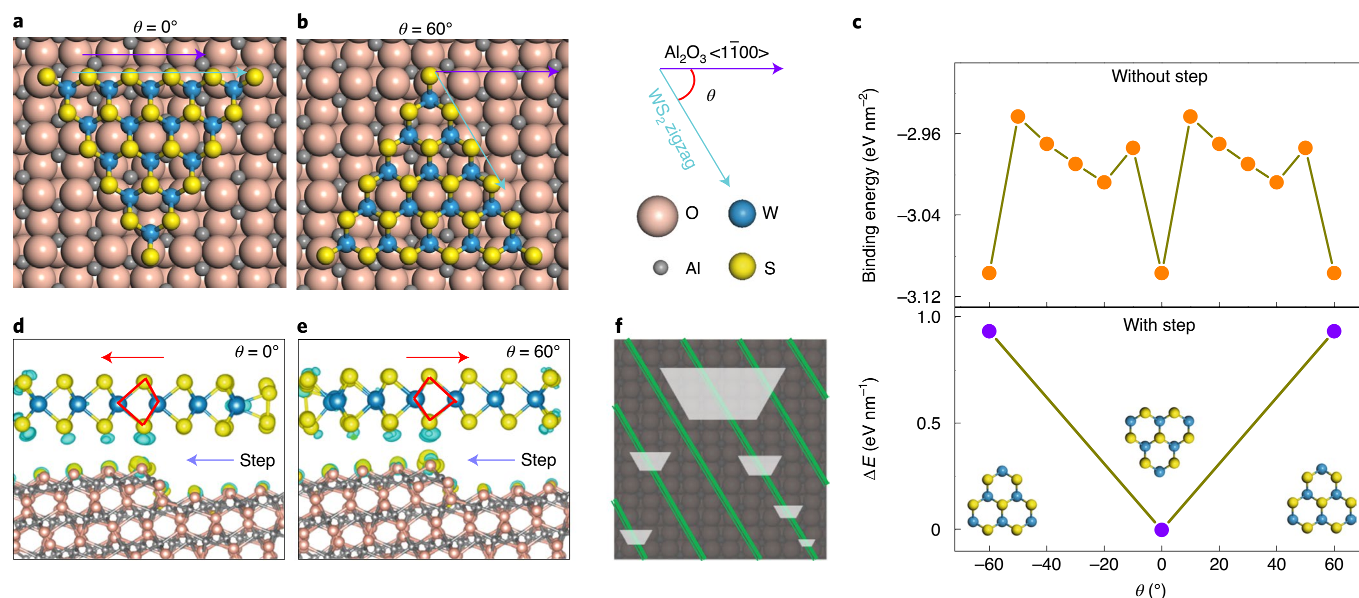

Fig. 4 | Dual-coupling-guided epitaxial growth of WS_2 monolayer on vicinal *a*-plane sapphire. **a**,**b**, Schematic of the configuration of WS_2 cluster on a flat *a*-plane sapphire surface for $\theta = 0°$ (**a**) and $\theta = 60°$ (**b**), where θ is the angle between one zigzag direction of WS_2 and the <1$\bar{1}$00> plane of the *a*-plane sapphire surface. **c**, Top: DFT calculations of the binding energies of a WS_2 triangular island with different rotation angles on the *a*-plane sapphire surface. The results show that the energy surface has two deep minima at $\theta = 0°$ and $\theta = \pm 60°$, which correspond to the configurations shown in **a**. Bottom: relative energy difference between two antiparallel WS_2 islands that cross a step edge on the *a*-plane sapphire surface due to symmetry breaking. **d**,**e**, Optimized structures of antiparallel WS_2 ribbons crossing an atomic step of *a*-plane sapphire (side view) for $\theta = 0°$ (**d**) and $\theta = 60°$ (**e**), in which the distributions of charge difference are also shown. The calculation showed that the binding energy between the step edge and WS_2 depends on its alignment and breaks the C_2 symmetry of the WS_2/*a*-plane sapphire system. Differences in the S-W-S bond direction are marked by red symbols and arrows. **f**, Schematic of WS_2 islands grown on *a*-Al_2O_3 during the early stage of growth. The driving force for both in-plane and edge coupling between WS_2 and sapphire leads to the unidirectional alignment of islands during the early growth stage.

a-Al_2O_3 surface to initiate the nucleation of WS_2 islands and break the degeneracy of the two antiparallel alignments of WS_2 islands on the ideal *a*-Al_2O_3 surface (Fig. 4d,e and Fig. 4c, bottom).

Quantitatively, our calculations estimate that the coupling strength between WS_2 and *a*-plane sapphire is ~200 meV per WS_2 formula unit, which is much larger than that on other insulating substrates (for example, ~80 meV per WS_2 formula unit for the (0001) surface of quartz). This relatively strong interaction is also demonstrated by the observed blue-shift in the PL peaks in as-grown WS_2 on *a*-Al_2O_3 (Supplementary Fig. 15c,d).

Furthermore, our DFT calculations clearly show that the interaction between WS_2 and step edge depends on the alignment of WS_2. Although two antiparallel WS_2 island crossing the step edge have almost the same shape, their interactions with the active step edge are fairly different (Fig. 4d,e). Therefore, the step edge reduces the symmetry of the substrate from C_2 to C_1, and makes it possible to have all the WS_2 islands aligned only along one direction. For a WS_2 island having a contact length of ~5 nm with the step edge, the energy difference (ΔE) between the two antiparallel WS_2 islands reaches ~4 eV and the preferred alignment has a thermodynamic probability of $1/\left(1+\exp\left(\frac{\Delta E}{k_B T}\right)\right) > 99.99\%$, where k_B is the Boltzmann constant and $T = 1{,}238$ K is the growth temperature. During the initial nucleation stage, the WS_2 islands nucleate at the active step edges, which, in turn, strongly interact with the WS_2 islands. The low symmetry of the sapphire step edge allows to differentiate the two antiparallel alignments of the WS_2 islands across it; finally, only WS_2 islands with one type of alignment survive (Fig. 4f).

This dual-coupling-guided growth mechanism should, in principle, be applicable to grow other single-crystal TMD materials on insulators as well. Here we have given the examples of the epitaxy of MoS_2, WSe_2 and $MoSe_2$ on *a*-Al_2O_3 (Supplementary Figs. 20–24). The successful growth of wafer-scale 2D TMD single crystals on insulating surfaces beyond graphene and hBN on transition metal surfaces provides the required cornerstone of 2D semiconductors in high-end applications of next-generation integrated optical and electronic devices.

Online content

Any methods, additional references, Nature Research reporting summaries, source data, extended data, supplementary information, acknowledgements, peer review information; details of author contributions and competing interests; and statements of data and code availability are available at https://doi.org/10.1038/s41565-021-01004-0.

Received: 8 December 2020; Accepted: 9 September 2021;
Published online: 15 November 2021

References

1. Wang, Q. H. et al. Electronics and optoelectronics of two-dimensional transition metal dichalcogenides. *Nat. Nanotechnol.* **7**, 699–712 (2012).
2. Radisavljevic, B. et al. Single-layer MoS_2 transistors. *Nat. Nanotechnol.* **6**, 147–150 (2011).
3. Mak, K. F., McGill, K. L., Park, J. & McEuen, P. L. The valley Hall effect in MoS_2 transistors. *Science* **344**, 1489–1492 (2014).
4. Jin, C. H. et al. Imaging of pure spin-valley diffusion current in WS_2-WSe_2 heterostructures. *Science* **360**, 893–896 (2018).
5. Xu, X. Z. et al. Ultrafast epitaxial growth of metre-sized single-crystal graphene on industrial Cu foil. *Sci. Bull.* **62**, 1074–1080 (2017).
6. Wang, L. et al. Epitaxial growth of a 100-square-centimetre single-crystal hexagonal boron nitride monolayer on copper. *Nature* **570**, 91–95 (2019).
7. Lee, J. S. et al. Wafer-scale single-crystal hexagonal boron nitride film via self-collimated grain formation. *Science* **362**, 817–821 (2018).

8. Chen, T. A. et al. Wafer-scale single-crystal hexagonal boron nitride monolayers on Cu (111). *Nature* **579**, 219–223 (2020).
9. Chen, L. et al. Step-edge-guided nucleation and growth of aligned WSe_2 on sapphire via a layer-over-layer growth mode. *ACS Nano* **9**, 8368–8375 (2015).
10. Chubarov, M. et al. Wafer-scale epitaxial growth of unidirectional WS_2 monolayers on sapphire. *ACS Nano* **15**, 2532–2541 (2021).
11. Lee, Y. H. et al. Synthesis of large-area MoS_2 atomic layers with chemical vapor deposition. *Adv. Mater.* **24**, 2320–2325 (2012).
12. Najmaei, S. et al. Vapour phase growth and grain boundary structure of molybdenum disulphide atomic layers. *Nat. Mater.* **12**, 754–759 (2013).
13. van der Zande, A. M. et al. Grains and grain boundaries in highly crystalline monolayer molybdenum disulphide. *Nat. Mater.* **12**, 554–561 (2013).
14. Zheng, J. et al. High yield exfoliation of two-dimensional chalcogenides using sodium naphthalenide. *Nat. Commun.* **5**, 2995 (2014).
15. Dumcenco, D. et al. Large-area epitaxial monolayer MoS_2. *ACS Nano* **9**, 4611–4620 (2015).
16. Gao, Y. et al. Large-area synthesis of high-quality and uniform monolayer WS_2 on reusable Au foils. *Nat. Commun.* **6**, 8569 (2015).
17. Zhou, J. D. et al. A library of atomically thin metal chalcogenides. *Nature* **556**, 355–359 (2018).
18. Yang, P. et al. Epitaxial growth of centimeter-scale single-crystal MoS_2 monolayer on Au (111). *ACS Nano* **14**, 5036–5045 (2020).
19. Li, J. et al. General synthesis of two-dimensional van der Waals heterostructure arrays. *Nature* **579**, 368–374 (2020).
20. Wang, Q. Q. et al. Wafer-scale highly oriented monolayer MoS_2 with large domain sizes. *Nano Lett.* **20**, 7193–7199 (2020).
21. Sang, X. H. et al. In situ edge engineering in two-dimensional transition metal dichalcogenides. *Nat. Commun.* **9**, 2051 (2018).
22. Kurita, T., Uchida, K. & Oshiyama, A. Atomic and electronic structures of α-Al_2O_3 surfaces. *Phys. Rev. B* **82**, 155319 (2010).
23. Dong, J. C., Zhang, L. N., Dai, X. Y. & Ding, F. The epitaxy of 2D materials growth. *Nat. Commun.* **11**, 5862 (2020).
24. Ismach, A., Segev, L., Wachtel, E. & Joselevich, E. Atomic-step-templated formation of single wall carbon nanotube patterns. *Angew. Chem. Int. Ed.* **43**, 6140–6143 (2004).
25. Cheng, J. X. et al. Chiral selection rules for multi-photon processes in two-dimensional honeycomb materials. *Opt. Lett.* **44**, 2141–2144 (2019).
26. Hong, J. H. et al. Exploring atomic defects in molybdenum disulphide monolayers. *Nat. Commun.* **6**, 6293 (2015).
27. Qiu, H. et al. Hopping transport through defect-induced localized states in molybdenum disulphide. *Nat. Commun.* **4**, 2642 (2013).
28. Wang, G. et al. In-plane propagation of light in transition metal dichalcogenide monolayers: optical selection rules. *Phys. Rev. Lett.* **119**, 047401 (2017).
29. Zeng, H. L. et al. Valley polarization in MoS_2 monolayers by optical pumping. *Nat. Nanotechnol.* **7**, 490–493 (2012).
30. Zhu, B. R. et al. Anomalously robust valley polarization and valley coherence in bilayer WS_2. *Proc. Natl Acad. Sci. USA* **111**, 11606–11611 (2014).
31. Scrace, T. et al. Magnetoluminescence and valley polarized state of a two-dimensional electron gas in WS_2 monolayers. *Nat. Nanotechnol.* **10**, 603–607 (2015).
32. Plechinger, G. et al. Trion fine structure and coupled spin-valley dynamics in monolayer tungsten disulfide. *Nat. Commun.* **7**, 12715 (2016).
33. Lu, J. M. et al. Evidence for two-dimensional Ising superconductivity in gated MoS_2. *Science* **350**, 1353–1357 (2015).

Publisher's note Springer Nature remains neutral with regard to jurisdictional claims in published maps and institutional affiliations.

© The Author(s), under exclusive licence to Springer Nature Limited 2021

Methods

Annealing of vicinal *a*-plane sapphire wafer in O_2 atmosphere. Vicinal *a*-plane sapphire wafer was specially ordered from a local company (Sichuan Oriental Stars Trading). To form uniform atomic steps on the entire wafer surface, the sapphire substrates were annealed at 1,140 °C in air for about 5 h.

Growth of single-crystal WS_2 monolayer on vicinal *a*-plane sapphire. The WS_2 monolayer films were grown on *a*-plane sapphire in a chemical vapour deposition (CVD) system with three temperature zones, namely, zones I–III. Sulfur (Alfa Aesar, 99.9%) powder was placed at the upstream end of a quartz tube and heated by a heating band. WO_3 (Alfa Aesar, 99.99%) powder and NaCl (Greagent, 99.95%) were placed in zone I of the tube furnace and sapphire substrates were placed in zone III. The CVD process was performed under low pressure in an argon (Ar) atmosphere. During the growth process, the temperature of the S source and the temperatures of zone I, zone II and zone III, were set at 125, 645, 850 and 965 °C, respectively, under a mixed-gas flow (Ar, 200 s.c.c.m.; H_2, 0–5 s.c.c.m.). The pressure in the growth chamber was kept at ~300 Pa. To obtain individual islands, the growth time was 5–20 min; for a continuous WS_2 film, the growth time was 1 h. After growth, the whole CVD system was cooled down to room temperature under an Ar gas flow (500 s.c.c.m.).

Growth of MoS_2, $MoSe_2$ and WSe_2 on vicinal *a*-plane sapphire. The growth recipes were very similar to that for WS_2, except for the replacement of WO_3 by MoO_3 source, S by Se source, and the temperature settings were accordingly adjusted. During MoS_2 growth, the temperature of the S source and temperatures of zone I, zone II and zone III were set at 125, 550, 850 and 965 °C, respectively, under an Ar gas flow (200 s.c.c.m.). During $MoSe_2$ growth, the temperature of the Se source and temperatures of zone I, zone II and zone III were set at 250, 550, 850 and 965 °C, respectively, under a mixed-gas flow (Ar, 200 s.c.c.m.; H_2, 5 s.c.c.m.). During WSe_2 growth, the temperature of the Se source and temperatures of zone I, zone II and zone III were set at 250, 645, 850 and 965 °C, respectively, under a mixed-gas flow (Ar, 160 s.c.c.m.; H_2, 40 s.c.c.m.).

Etching of WS_2 film to visualize grain boundaries. After growth, a mixed-gas flow comprising Ar and O_2 was introduced into the CVD system (Ar, 200 s.c.c.m.; O_2, 1–10 s.c.c.m.) for 5–30 min to etch holes in the continuous WS_2 film. By changing the O_2 concentration, temperature and etching time, the shape of the etched holes could be tuned from hexagonal to trapezoidal. To visualize the grain boundaries by optical microscopy, the as-grown large-area continuous WS_2 film was exposed to hot water vapour at 70 °C for 20 h to etch the defective grain boundaries.

Characterization.

(1) LEED measurements were performed using an Omicron LEED system in an ultrahigh vacuum with a base pressure of $<3\times10^{-7}$ Pa. Scanning electron microscopy (SEM) images were obtained using an FEI Nova NanoSEM 430 instrument. AFM measurements were performed using Asylum Research Cypher under ambient conditions.

(2) Optical measurements. Raman spectra were obtained with a home-made Raman system with a laser excitation wavelength of 532 nm and power of ~0.5 mW. Low-temperature PL spectra were obtained at 7.5 K using a home-made optical cryostat with a laser excitation wavelength of 532 nm and power of ~8 μW. Circular helicity of the films was probed under an off-resonant excitation photon energy of 2.34 eV. Polarized light was generated with a super-achromatic quarter-wave plate (Thorlabs SAQWP05M-700) and the PL was analysed through the same quarter-wave plate as well as a linear polarizer. SHG mapping was obtained using the same system under excitation from a femtosecond laser centred at 820 nm with an average power of 800 μW (Spectra-Physics InSight system with a pulse duration of 200 fs and repetition rate of 80 MHz). We used circularly polarized light to excite the SHG, and grain boundaries were visualized as dark lines in SHG imaging[25].

(3) TEM characterization. The WS_2 (MoS_2) sample for TEM characterization was prepared by transferring WS_2 (MoS_2) onto home-made monolayer graphene TEM grids using the polymethyl-methacrylate-based transfer technique. Graphene TEM grids were made by transferring large-area monolayer single-crystal graphene on commercial holey carbon TEM grids (Zhongjingkeyi GIG-2010-3C). Scanning transmission electron microscopy (STEM) experiments were performed using an FEI Titan Themis G2 300 system operated at 300 kV and a Nion U-HERMES200 system at 60 kV.

(4) X-ray diffraction measurements were conducted using a PANalytical Empyrean system with a copper target.

Computational details. Geometric optimization and energy calculations of WS_2/*a*-Al_2O_3 systems were carried out using DFT calculations as implemented in the Vienna ab initio simulation package[34,35]. The Perdew–Burke–Ernzerhof functional with the generalized gradient approximation was adopted to treat the exchange–correlation functional[36]. To include van der Waals interactions between WS_2 and the substrate, the widely used dispersion-corrected DFT-D3 method was chosen[37]. A plane-wave basis energy cutoff of 400 eV was used; the energies and forces were set to converge below a threshold of 10^{-4} eV and 0.01 eV Å^{-1}, respectively, to fully relax the structures in all the calculations. We chose the Gaussian smearing method. We constructed triangular WS_2 clusters (57 atoms) on *a*-Al_2O_3 with oxygen termination (stoichiometric surfaces, 360 atoms) and the size of the unit cell was 25.98 Å × 24.73 Å. Some atomic layers of *a*-Al_2O_3 were frozen (marked in Supplementary Fig. 25) to represent the sapphire surface, and a 1 × 1 × 1 Monkhorst–Pack *k*-point mesh was adopted. The binding energies of the WS_2–substrate hybrid, namely, $E_b = (E_{hyb} - E_{WS2} - E_{sub})/S$, was calculated using the relaxed structures, where E_{hyb} is the total energy of the hybrid; E_{WS2} and E_{sub} represent the energies of WS_2 and the substrate, respectively; and S is the area of the WS_2 cluster. To estimate the sapphire step–WS_2 interaction, two antiparallel WS_2 nanoribbons with a length of about 1.7 nm (100 atoms) were placed on the <1$\bar{1}$01> step of the vicinal *a*-Al_2O_3 surface (358 atoms) and then relaxed; the size of sapphire was 15.64 Å × 24.47 Å. The energy difference was defined as $\Delta E = (E_1 - E_2)/L$, where E_1 and E_2 are the total energies of the hybrid system, respectively, and L is the length of the nanoribbon. Similar calculations were also conducted for the MoS_2/*a*-Al_2O_3 systems.

To understand the formation mechanism of the trapezoidal shape of the WS_2 island, we modelled the diffusion of the S_2 dimer on the *a*-plane surface of sapphire, and the energy barrier of each reaction was calculated using the climbing image nudged elastic band approach[38]. To understand the seamless stitching of the islands energetically, we modelled two possible cases of the stitching of two WS_2 islands (the length of one island is 16.53 nm) when they are away from each other with a WS_2 lattice constant of 1/2: (1) forming a line defect (5588 type) and (2) well-aligned structure with evenly distributed strain. The formation energy of the strained model is calculated as $E_{strained} = 1/2 \times C_{11} \times L \times h \times \varepsilon^2$, where $C_{11} = 149$ J m^{-2}, $h = 0.64$ nm and ε is the applied strain.

Data availability

Source data are provided with this paper. The data that support the findings of this study are available within the paper and Supplementary Information. Additional data are available from the corresponding authors upon reasonable request.

References

34. Kresse, G. & Furthmuller, J. Efficiency of ab-initio total energy calculations for metals and semiconductors using a plane-wave basis set. *Comp. Mater. Sci.* **6**, 15–50 (1996).
35. Kresse, G. & Furthmuller, J. Efficient iterative schemes for ab initio total-energy calculations using a plane-wave basis set. *Phys. Rev. B* **54**, 11169–11186 (1996).
36. Perdew, J. P., Burke, K. & Ernzerhof, M. Generalized gradient approximation made simple. *Phys. Rev. Lett.* **77**, 3865–3868 (1996).
37. Grimme, S., Antony, J., Ehrlich, S. & Krieg, H. A consistent and accurate ab initio parametrization of density functional dispersion correction (DFT-D) for the 94 elements H-Pu. *J. Chem. Phys.* **132**, 154104 (2010).
38. Henkelman, G., Uberuaga, B. P. & Jonsson, H. A climbing image nudged elastic band method for finding saddle points and minimum energy paths. *J. Chem. Phys.* **113**, 9901–9904 (2000).

Acknowledgements

This work was supported by the National Natural Science Foundation of China (52025023 (K.L.), 51991342 (K.L.), 52021006 (K.L.), 11888101 (E.W.) and 52102043 (X.X.)); the Key R&D Program of Guangdong Province (2020B010189001 (X.X.), 2019B010931001 (K.L.) and 2018B030327001 (D.Y.)); Science and Technology Program of Guangzhou (2019050001 (X.X.)); the Pearl River Talent Recruitment Program of Guangdong Province (2019ZT08C321 (X.X.)); Beijing Natural Science Foundation (JQ19004 (K.L.)); Guangdong Provincial Science Fund for Distinguished Young Scholars (2020B1515020043 (X.X.)); National Key R&D Program of China (2016YFA0300903 (K.L.), 2016YFA0300804 (P.G.) and 2019YFA0307800 (L.L.)); Guangdong Innovative and Entrepreneurial Research Team Program (2016ZT06D348 (D.Y.)); the Science, Technology and Innovation Commission of Shenzhen Municipality (KYTDPT20181011104202253 (D.Y.)); the Strategic Priority Research Program of Chinese Academy of Sciences (XDB33000000 (K.L.)); National Postdoctoral Program for Innovative Talents (BX20190016 (C.L.)); China Postdoctoral Science Foundation (2019M660280 (C.L.), 2019M660281 (R.Q.) and 2020T130022 (R.Q.)); and the Institute for Basic Science (IBS-R019-D1 (F.D.)), South Korea. The authors also acknowledge the use of the IBS-CMCM high-performance computing system simulator.

Author contributions

K.L. conceived and supervised the project. J.W., X.X., Z.L., P.Z., G.C., C.C., C.L., Y. Zuo, G.X., M.W. and E.W. performed the sample growth. T.C. and F.D. performed the theoretical calculations. L.G., H.H., C.H., J. Liang, Z.T. and S.W. conducted the optical

measurements. R.Q., Y.G., D.Y. and P.G. conducted the TEM measurements. D.D., J.T., Z.Y., L.L., R.Y., G.Z. and J. Lu conducted the electrical measurements. Zhibin Zhang, Zhihong Zhang, S.Z., J.Q., Y. Zhao, Q.J. and Q.L. conducted the AFM measurements. X.X. and X.F. conducted the LEED measurements. All the authors discussed the results and wrote the manuscript.

Competing interests

The authors declare no competing interests.

Additional information

Supplementary information The online version contains supplementary material available at https://doi.org/10.1038/s41565-021-01004-0.

Correspondence and requests for materials should be addressed to Yun Zhao, Shiwei Wu, Feng Ding or Kaihui Liu.

Peer review information *Nature Nanotechnology* thanks Xiangfeng Duan and the other, anonymous, reviewer(s) for their contribution to the peer review of this work.

Reprints and permissions information is available at www.nature.com/reprints.